NASA TECHNICAL NOTE

NASA TN D-5303

$C.\ 1$

APPLICATION OF A DOUBLE-DEAD-TIME MODEL DESCRIBING CHUGGING TO LIQUID-PROPELLANT ROCKET ENGINES HAVING MULTIELEMENT INJECTORS

by John R. Szuch

Lewis Research Center
Cleveland, Ohio

NATIONAL AERONAUTICS AND SPACE ADMINISTRATION • WASHINGTON, D. C. • JULY 1969

APPLICATION OF A DOUBLE-DEAD-TIME MODEL DESCRIBING

CHUGGING TO LIQUID-PROPELLANT ROCKET ENGINES

HAVING MULTIELEMENT INJECTORS

By John R. Szuch

Lewis Research Center
Cleveland, Ohio

ABSTRACT

Stability limits were determined experimentally for a 1.4-inch- (3.56-cm-) diameter rocket engine. Liquid oxygen and gaseous hydrogen were the propellants. A chamber pressure of 250 psia (172 N/cm^2) and a mixture ratio of 5.0 were maintained for contraction ratios of about 1.9 and 3.0. A seven-element injector was run with both concentric-tube and transpiration-cooled faceplate methods of fuel injection. Data were also obtained with a 421-element 10.8-inch- (27.4-cm-) diameter engine. For comparison with experimental data, stability boundaries were generated on the analog computer. Results indicated that accurate predictions of stability limits can be made using the double-dead-time model and existing vaporization and drop-size correlations. Large engine instabilities were prevented because of feed system coupling effects, as predicted by the analysis.

APPLICATION OF A DOUBLE-DEAD-TIME MODEL DESCRIBING

CHUGGING TO LIQUID-PROPELLANT ROCKET ENGINES

HAVING MULTIELEMENT INJECTORS

by John R. Szuch

Lewis Research Center

SUMMARY

One of the more serious problems encountered when operating liquid-propellant rocket engines is the occurrence of low frequency instabilities, commonly referred to as chugging. The purpose of this investigation is to test the applicability of a double-dead-time model to typical injector-chamber configurations. Tests were conducted on both a seven-element 1.4-inch- (3.56-cm-) diameter chamber and a 421-element 10.8-inch- (27.4-cm-) diameter chamber. Both concentric-tube and transpiration-cooled faceplate injection techniques were studied. The propellants were gaseous hydrogen and liquid oxygen, both at 140° R (77.8 K). A nominal oxidant-fuel mixture ratio of 5.0 and a chamber pressure of 250 psia (172 N/cm^2) were maintained for contraction ratios of about 1.9 and 3.0.

Injector pressure drop requirements for stability were determined for all configurations. For comparison with experimental results, stability limits were determined using an analog computer simulation. Good agreement between experimental and computer limits was obtained for all subscale configurations. Large-engine instabilities were prevented because of feed system coupling effects, as predicted by the analysis.

Vaporization time was found to be a strong function of fuel velocity for both concentric-tube and transpiration-cooled faceplate injection. An attempt was made to relate gas-phase "mixing delay time" to measurable engine quantities using all available chugging data with these propellants.

INTRODUCTION

One of the more serious problems encountered when operating liquid-propellant rocket engines is the occurrence of low frequency instabilities, commonly referred to as

chugging. Chugging is generally caused by a coupling of the propellant feed system with the combustion chamber dynamics in such a way as to reinforce any disturbance in pressure or propellant flow. Many analyses of chugging (refs. 1 to 3) have shown that the controlling factors in determining low frequency stability are the time delays associated with the atomization, vaporization, and combustion processes. Without these delays, the injector-chamber system would be inherently stable.

The most commonly used technique for analyzing chugging in a bipropellant rocket engine is to compute the time delay associated with the propellant having the longest drop lifetime and then to apply this delay to both propellants (ref. 4). However, experimental results reported in reference 5 have shown that this approach does not, in general, adequately describe the dynamic behavior of a bipropellant system over a wide range of engine operation. By computing the time delays for both propellants and by applying them to their respective flows, one can accurately predict the occurrence of multiple frequency instabilities and of irregularities in the injector pressure drop limits. This approach, which is referred to as the "double-dead-time model," is developed in reference 6. The double-dead-time model has correctly predicted the stabilization of a liquid oxygen - gaseous hydrogen combustor by decreasing the fuel injector pressure drop as reported in reference 5.

The experimental data, reported in reference 5, were obtained with a single-element injector. In addition, the hydrogen was at ambient temperature and was injected through a transpiration-cooled faceplate. To conform more nearly with engines currently in development, the testing reported herein was conducted on multiple-element, concentric-tube injectors with the hydrogen at liquid nitrogen temperature (140° R, 77.8 K).

Experiments were conducted at the NASA Lewis Research Center. A subscale engine configuration, consisting of a seven-element injector and a 1.4-inch- (3.56-cm-) diameter chamber, was run with contraction ratios of 1.96 and 3.02. The chamber length was 11.5 inches (29.2 cm). To test the applicability of current analytical models to large engines, a full-scale configuration with a 421-element 10.8-inch- (27.4-cm-) diameter chamber and chamber lengths of 5.0 and 10.5 inches (12.7 and 26.7 cm) was also run. Both subscale and full-scale engines were run at a nominal chamber pressure of 250 psia (172 N/cm^2) with an oxidizer-fuel mixture ratio of 5.0.

Transitions from stable to unstable operation were accomplished by varying the injector pressure drops while maintaining the same propellant flow rates - hence, chamber pressure. To conform with the assumption of time-invariant injector pressures (ref. 6), attempts were made to design the injectors with high manifold capacitance. Stability limits were determined for all configurations and compared with results from an analog computer simulation.

APPARATUS

Injector

A cutaway drawing of the subscale injector is shown in figure 1. To conform with the assumption of time-invariant injector pressures, sufficient injector-fluid capacitance had to be maintained in the propellant manifold volumes. On the hydrogen side, this capacitance was provided by adding a large volume (300 in.^{3}, 4920 cm^3) immediately upstream of the injector. On the oxygen side, due to the high bulk modulus of the liquid, the capacitance had to be provided mechanically. The flexible diaphragm was designed with sufficient flexibility to provide the required capacitance. The dome volume was pressurized, prior to running, to the anticipated injector pressure minus about 15 psi (10.3 N/cm^2) to give the optimum diaphragm deflection. The supporting plate was necessary to give support to the diaphragm under this preload condition.

The oxidizer injector pressure drop was varied by changing the flow diameter of the removable sharp-edged orifice. Flow diameters ranging from 0.136 to 0.265 inch (0.345 to 0.673 cm) were used. The oxidizer manifold volume, immediately upstream of the injector elements, was made sufficiently small (1 in.^{3}, 16.4 cm^3) so that the orifice could dynamically be considered part of the injector elements over the frequency range of interest.

The fuel injector pressure drop was varied by changing the annulus diameter of the removable copper faceplate. Total fuel annulus areas ranging from 0.0226 to 0.144 square inch (0.146 to 0.998 cm^2) were provided by using annulus diameters between 0.140 and 0.204 inch (0.356 and 0.518 cm), respectively.

For comparison with the concentric-tube injection of hydrogen, transpiration-cooled faceplates were also run. Faceplates of varying porosity were selected to give the desired range of injector pressure drop for the specified hydrogen flow rates.

Figure 2 shows the injector element detail for both the subscale and full-scale injectors. Since both configurations were run with the same propellant flow per element, the different element diameters were used to investigate the effect of propellant injection velocity on stability.

Figure 3 shows a schematic representation of the full-scale injector and feed system. The oxidizer injector manifold volume was made less than 50 cubic inches (819 cm^3) so that the variable-area valve could dynamically be considered part of the injector. Variations in the oxidizer pressure drop were accomplished by changing the flow area of the valve. In an attempt to both decouple the remainder of the oxidizer feed system from the injector and to study the effect of injector capacitance on stability, a standpipe was located just upstream of the valve and downstream of the high ΔP fire valve. Initial testing was conducted with an unpressurized 775-cubic-inch (1.27×10^4 cm^3) standpipe. Later

3

attempts at feed system isolation were made with a 5875-cubic-inch (0.63×10^4-cm^3) volume, prepressurized with nitrogen gas at ambient temperature.

Engine

Uncooled combustion chambers were used. The subscale engine chamber had an inside diameter of 1.4 inches (3.56 cm) with a chamber length of 11.5 inches (29.2 cm). The full-scale engine chamber had an inside diameter of 10.8 inches (27.4 cm) and was run with both 5.0- and 10.5-inch (12.7- and 26.7-cm) chamber lengths. The shorter chamber provided a smaller gas residence time and was run in an attempt to cause instability.

With a nominal chamber pressure of 250 psia (172 N/cm^2) and an oxidizer-fuel mixture ratio of 5.0, both configurations were run with contraction ratios of about 1.9 and 3.0. For the subscale engine, these values were provided by nozzle throat diameters of 1.00 and 0.805 inch (2.54 and 2.04 cm), respectively. For the full-scale engine, throat diameters of 7.85 and 6.23 inches (19.9 and 15.8 cm) were required. The higher contraction ratio was run to both test the analytical models currently in use and to decrease the propellant flow rates in an attempt to cause instability.

Instrumentation

For all tests, the oxidizer flow rate was measured by means of turbine-type flowmeters located upstream of the injector manifolds. Gaseous hydrogen flow rate was measured with a critical-flow venturi. All steady-state pressures were measured with strain-gage-type transducers. For subscale tests, dynamic pressure measurements were made in the chamber and in the injector cavities using piezoelectric transducers. For the full-scale tests, three dynamic pressure measurements were made in the chamber. The measured parameters were recorded, for all tests, on galvonometric oscillographs. In addition, the data from full-scale testing were recorded on a high-speed digital recorder for computer processing. Outputs from all dynamic pressure transducers were recorded on FM tape recorders for later analysis.

PROCEDURE

Subscale Testing

Cold flow tests were conducted prior to initiating the stability investigation. The

purpose of these tests was to facilitate the analytical modeling of the injectors and to aid in establishing an experimental plan for both subscale and full-scale testing.

With no hydrogen flow, liquid oxygen (140° R, 77.8 K) was flowed through the injector. Figure 4 shows the resultant injector pressure drop plotted against oxidizer flow rate for orifice diameters of 0.136, 0.172, and 0.218 inch (0.345, 0.437, and 0.554 cm). By assuming an orifice flow coefficient of 0.6, one can calculate the percentage of the total injector pressure drop contributed by the elements. For an oxidizer flow per element of 0.10 pound per second (0.0454 kg/sec), the element pressure drop was calculated to be 30 psi (20.7 N/cm^2). For an oxidizer flow per element of 0.0629 pound per second (0.0285 kg/sec), the pressure drop across the elements would be 12 psi (8.27 N/cm^2). These values define the lower limit of the injector pressure drop at these flow rates and agree with pressure drop measurements made during the hot run phase of the program.

With no oxygen flow, gaseous hydrogen (140° R, 77.8 K) was exhausted through the injector annuli to the atmosphere. Figure 5 shows a plot of hydrogen injector pressure as a function of total hydrogen flow rate for annulus diameters ranging from 0.141 to 0.194 inch (0.358 to 0.493 cm). Because of the compressibility of the hydrogen, the data had to be corrected for an anticipated back pressure (chamber pressure) of 250 psia (172 N/cm^2). Assuming isentropic flow through the annulus, one can solve for the required pressure ratio (hence, injector pressure) across the injector to give the specified flow rate through a given annulus area. Figure 6 gives the plot of required hydrogen injector pressure as a function of annulus diameter for total hydrogen flow rates of 0.140 and 0.083 pound per second (0.0636 and 0.0377 kg/sec). Also shown are the required pressures, assuming isothermal flow through the injector.

Subscale engine operation was completely open loop; that is, the propellant supply pressures had to be manually set, prior to running, to values which hopefully would produce the desired chamber pressure and mixture ratio. If the resultant conditions proved unsatisfactory, the pressures had to be readjusted prior to the next run.

With the ignition sequence controlled by an electric timer, the engine was fired for approximately 4 seconds. The timing was adjusted to give both smooth engine starting and about 2 seconds of steady-state operation. For each available annulus area, the engine was run with different orifice sizes, starting with the smallest until a transition from stable to unstable operation was observed. This procedure was then repeated for all available transpiration-cooled faceplates. Stability data were taken at contraction ratios of 1.96 and 3.02.

Full-Scale Testing

Although the subscale testing provided an accurate calibration of injector pressure

drop against annulus area for the hydrogen injector, cold flow tests had to be conducted to determine oxygen injector pressure drop as a function of the preset position of the variable-area valve (see fig. 3). With no hydrogen flow, liquid oxygen (140° R, 77.8 K) was flowed through the injector with various preset pressures on the valve. Figure 7 shows the resultant valve calibration for total oxygen flow rates of 42.1 and 26.5 pounds per second (19.1 and 12 0 kg/sec).

Full-scale engine operation was closed loop. That is, the fire valve stem positions were determined by the measured values of chamber pressure and mixture ratio.

Initial full-scale testing was done with a contraction ratio of 1.90, a 10.5-inch (26.7-cm) chamber length, and a 0.152-inch (0.386-cm) annulus diameter. The 775-cubic-inch (1.27×10^4 cm^3) standpipe (see fig. 3) was used with the variable-area valve set at its desired setting. The engine ignition sequence and valve timing were set to give about 2 seconds of steady-state operation. Runs were made with valve pressures of 8, 9, 10, and 16 psi (5.5, 6.2, 6.9, and 11 N/cm^2). The highest setting corresponded to the minimum attainable injector pressure drop at the prescribed flow rates. In an attempt to cause instability, the procedure was repeated, with a contraction ratio of 2.84 and a chamber length of 5.0 inches (12.2 cm), with both 0.152- and 0.140-inch (0.386- and 0.356-cm) annulus diameters. Final attempts at causing instability by decoupling the injector and oxidizer feed system were made by installing the 5875-cubic-inch (9.63×10^4 cm^3) standpipe. If both the fire valve and variable-area valve were initially closed, the standpipe could be pressurized to about 250 psia (172 N/cm^2) with nitrogen gas at ambient temperature. After initiating the run by opening both valves, it was hoped to have a sufficient volume of gas at the standpipe to provide sufficient capacitance at that point to attenuate any injector pressure oscillations at the frequencies of interest (100 to 300 Hz). Under these conditions, runs were made with the variable-area valve at its fully open position (16 psi, 11 N/cm^2, setting) and a 0.140-inch (0.356-cm) annulus diameter.

RESULTS AND DISCUSSION

Subscale Test Results

A total of 38 experimental runs was made with the seven-element, concentric-tube injector and a contraction ratio of 1.96. This configuration is referred to as configuration A, and pertinent data for these runs are given in table I. In general, the transition from stable to unstable operation was rather abrupt, indicating a small variance in the size of injected droplets (hence, vaporization rates). Results obtained with a single-element, transpiration-cooled injector (ref. 5) indicated an unusually high drop-size variance with that injector.

A convenient way of plotting the stability data is to plot the ratios of injector pressure drop to chamber pressure (ref. 6). The chamber pressure at the inlet to the exhaust nozzle P_t is used and is computed from the chamber pressure measured at the injector face as follows:

$$\epsilon_c = \frac{1}{M_1} \left(\frac{1 + \frac{\gamma - 1}{2} M_1^2}{1 + \frac{\gamma - 1}{2}} \right)^{(\gamma+1)/2(\gamma-1)} \tag{1}$$

$$\frac{P_c}{P_t} = \frac{1 + \gamma M_1^2}{\left(1 + \frac{\gamma - 1}{2} M_1^2\right)^{\gamma/(\gamma-1)}} \tag{2}$$

All symbols are defined in appendix A.

Figure 8(a) shows a plot of the 38 data points for configuration A. The observed frequencies are noted for those runs where unstable, high amplitude oscillations were observed. A stability boundary has been drawn between the stable and unstable runs. The region to the right of the boundary corresponds to stable operation, while the region to the left is unstable. The shape of the stability boundary is such that a decrease in the fuel injector ΔP can stabilize the engine. For example, a decrease in the fuel injector pressure drop ratio from 0.72 to about 0.5 at an oxidizer injector pressure drop ratio of 0.27 stabilizes the engine. This behavior is characteristic of the double-dead-time model (ref. 6). There is also a decrease in the observed frequencies along the boundary as the fuel injector pressure drop is decreased, indicating a sensitivity of combustion delay to the fuel velocity.

Seventeen experimental runs were made with the seven-element, concentric-tube injector and a contraction ratio of 3.02. Pertinent data for these runs are given in table II. Figure 8(b) shows a plot of these data and the inferred stability boundary. This configuration is referred to as configuration B. As in the case of configuration A, an abrupt transition from stable to unstable operation was observed. Also, stabilization with decreasing fuel injector ΔP and a decrease in frequency along the boundary were observed. Somewhat lower frequencies than those observed with configuration A were obtained. In addition, the three runs with a fuel injector $\Delta P/P_t$ less than 0.15 had chamber pressure oscillations at more than one frequency, which indicates the existence of a higher frequency boundary intersecting the lower frequency boundary. Based on results given in reference 5, a portion of the higher frequency boundary has been drawn in figure 8(b).

Nine experimental runs were made with the seven-element, transpiration-cooled injector and a contraction ratio of 1.96. Data for these runs are given in table III, and this configuration is referred to as configuration C. Figure 8(c) shows the nine data points and the inferred stability boundary. The half-shaded data points indicate a transitional condition which could be considered marginally stable. The same behavior as observed with the concentric-tube injector was encountered with somewhat lower frequencies noted, indicating higher values for combustion delay.

Twenty runs were made with the seven-element transpiration-cooled injector with a contraction ratio of 3.02. This configuration, referred to as configuration D, is described in table IV and figure 8(d). As noted with the other subscale configurations, configuration D exhibited sharp transitions from stable to unstable operation, stabilization with decreasing fuel injector ΔP and decreasing chugging frequency for decreasing fuel injector pressure drop (velocity). In addition, all but one of the unstable runs at fuel injector pressure ratios below 0.15, exhibited higher frequency content (about 400 Hz). This characteristic has been observed in previous studies conducted with these propellants (refs. 5 and 7) and was also observed with configuration B. As in figure 8(b), a portion of the higher frequency boundary has been drawn, intersecting the lower frequency boundary.

Full-Scale Test Results

Ten experimental runs were made with the 421-element, concentric-tube injector and the 775-cubic-inch $(1.27\times10^4\text{-}cm^3)$ oxidizer injector standpipe (see fig. 3). Four runs were made with a contraction ratio of 1.90 and an annulus diameter of 0.152 inch (0.386 cm). The chamber length was 10.5 inches (26.7 cm). This configuration is referred to as configuration E. Pertinent data for these runs are given in table V. Although these runs were stable, some 300-hertz content was noted in the dynamic chamber pressure measurements. As outlined in the ANALYSIS section (p. 9), this frequency was much higher than anticipated, leading one to investigate the effects of the feed system response on injector pressure drop limits and chugging frequency.

In an attempt to destabilize the engine, the contraction ratio was increased to 2.84. The annulus diameter was kept at 0.152 inch (0.386 cm) while three runs were made with various oxidizer injector pressure drops (control valve positions). This configuration is referred to as configuration F, and the pertinent data are given in table V.

Because of the reduced propellant flow rates, both the fuel injector pressure drop (about 32 percent of chamber pressure) and the allowable range of oxygen injector pressure drop were lower than those obtained with configuration E. These runs were also stable with the only high amplitude oscillations occurring during the shutdown transient. Those oscillations were at a frequency of 250 hertz (again, higher than anticipated).

The next step in trying to obtain instability was to shorten the chamber length to 5.0 inches (12.7 cm) and to decrease the annulus diameter to 0.140 inch (0.356 cm). The shorter chamber would result in a smaller value of the engine time constant θ_g - hence, higher engine gain at all frequencies. Based on the analysis in reference 6 and the experimental data in reference 5, the higher fuel injector pressure drop with the smaller annulus area could possibly destabilize the engine. This configuration is referred to as configuration G, and the data for the three runs made with it are given in table V. Again, all runs were stable, raising some doubt as to the effectiveness of the 775-cubic-inch $(1.27 \times 10^4 - cm^3)$ standpipe in decoupling the oxidizer fire valve (fig. 3) from the injector.

From the results of the analog computer simulation, which is described in the ANALYSIS section (p. 9), the oxidizer fluid - injector capacitance was found to have a profound effect on both the injector pressure drop limits and the chugging frequencies on the stability boundaries. The calculation of injector capacitance for both the 775- and 5875-cubic-inch $(1.27 \times 10^4 -$ and $9.63 \times 10^4 - cm^3)$ standpipes is given in appendix B. Briefly, the results of that analysis indicate that the larger standpipe would provide sufficient capacitance to destabilize the full-scale engine at low oxidizer injector presure drops.

Finally, two runs were made with configuration H, which consists of a 0.140-inch- (0.356-cm-) fuel annulus diameter, a contraction ratio of 2.84, a chamber length of 10.5 inches (26.6 cm), and the large standpipe volume. The resultant runs were also stable, with very low (30 Hz) frequencies observed in the dynamic chamber pressure signal. Pertinent data for these runs are given in table V. The existence of the low frequency content led to an investigation of the effect of standpipe geometry on the inductance (hence, resonant frequency) of the standpipe. This analysis is also given in appendix B. Briefly, the results indicate that the standpipe geometry is such that, although enough capacitance is provided, the inductance of the standpipe causes the injector to have a very low impedance (resonant condition) at about 20 hertz, but a much higher impedance at the frequencies where the chamber tends to oscillate. In effect, the high ΔP oxidizer fire valve was decoupled from the engine at 30 hertz, but coupled at the frequencies of interest (100 to 300 Hz).

ANALYSIS

Calculation of Combustion Delay Times

For comparison with the experimental results, both the subscale and full-scale configurations were simulated on the analog computer. The values for combustion delay used in the simulation were computed using the vaporization model of Priem and Heidmann (ref. 8). By assuming that vaporization is the rate-controlling combustion

process, the authors calculate vaporization rates and droplet histories for various pro-
pellant spray conditions and operating parameters. The results are correlated with an
effective chamber length for design purposes. The resultant correlation is of the form

$$l_{eff} = \left(\frac{l_c}{\epsilon_c^{0.44}} + \frac{0.83\, l_n}{\epsilon_c^{0.22} g^{0.33}}\right) \frac{\left(\dfrac{P_c}{300}\right)^{0.66}}{\left(1 - T_r\right)^{0.4}\left(\dfrac{\bar{d}_D}{0.006}\right)^{1.45}\left(\dfrac{v_i}{1200}\right)^{0.75}} \tag{3}$$

Figure 9 shows a plot of the percent of an injected oxygen droplet's mass vaporized
within a given chamber nozzle as a function of the effective length parameter l_{eff}
(ref. 8). For the case of a completely vaporized fuel, the combustion efficiency can be
related to the fraction of oxidizer vaporized (ref. 8) by

$$\eta = \frac{C_{th}^{*'}}{C_{th}^{*}} \frac{(r' + 1)}{(r + 1)} \tag{4}$$

The least known of the parameters that appear in the Briem-Heidmann correlation
is the mean drop diameter $\bar{d}_D$. If available performance data are fitted, using the cor-
relation equation, the required mean drop size can be calculated for a particular oper-
ating condition. Values of drop size for various injection spray patterns are given in
reference 8. However, these values do not satisfy the observed efficiencies for
concentric-tube injection of propellants (ref. 9) and the apparent sensitivity of combus-
tion delay to injection velocity observed in this study. The following equation is pre-
sented by Hersch and Rice in reference 9, and it relates the mean droplet diameter to
element size and propellant momentum ratio for a concentric-tube injector:

$$\bar{d} = C_{CT} d_j \left(\frac{\dot{w}_j v_j}{\dot{w}_a v_a}\right)^{1/2} = C_{CT}\, d_j r^{1/2}\left(\frac{v_j}{v_a}\right)^{1/2} \tag{5}$$

The effective length, as defined by Priem and Heidmann, must be converted to an
effective vaporization time to implement the stability model on the computer. Heidmann
and Wieber (ref. 10) have been able to correlate frequency response data obtained with
the Priem-Heidmann model with that obtained using a pure time delay to represent the
vaporization process. The required time dalay is equal to the time required to vaporize
50 percent of the mass of an injected droplet. For oxygen (see fig. 9) the effective length

10

required is 0.88 inch (0.224 cm). The droplet histories, presented in reference 8, indicate that the average droplet velocity over this length is very nearly equal to the injection velocity. This allows one to compute the time required to vaporize 50 percent of the mass of an injected oxygen droplet from

$$\tau_v = \tau_{50} = \frac{l_{50}}{v_i} \tag{6}$$

Vaporization times were calculated, using the digital computer, for all experimental runs. Since all runs were made at approximately the same chamber pressure, mixture ratio, and propellant inlet temperature, variations in delay were due only to changes in contraction ratio and fuel injector geometry (injection velocities and drop size). Based on observed C^* efficiencies, an average Hersch-Rice drop-size coefficient of 0.236 was calculated from all experimental runs. Figure 10 shows the resultant plot of calculated vaporization time as a function of fuel injector pressure drop ratio for both contraction ratios. Since the data could be fit approximately by one curve, the vaporization delay was assumed to be statically sensitive only to changes in fuel injector $\Delta P/P_t$ for the analog computer simulation.

In addition to the vaporization time delay, another determining factor in the stability of a liquid bipropellant engine system is the mixing and reaction time common to both propellant flows after vaporization. The method used to determine the value of this delay was to analyze data points observed to be near a stability boundary (neutrally stable). That value of mixing time which satisfied the phase angle conditions for neutral stability at the observed oscillatory frequency was assumed to apply for all data obtained with the same engine configuration. This procedure was applied to data obtained with both contraction ratios, using the characteristic equation for the system (ref. 6) and the digital computer. Mixing times of 0.2 and 0.5 millisecond were obtained for contraction ratios of 1.9 and 3.0, respectively, and were found to be the same for both concentric-tube and transpiration-cooled faceplate injection.

An attempt was made to correlate mixing and reaction times, calculated using this procedure, with a selected engine parameter. Figure 11 shows the resultant plot for all available data obtained with gaseous hydrogen - liquid oxygen propellants. Although these data are at different chamber pressures, it is felt that contraction ratio (hence, gas velocity) is the dominant factor in determining the mixing "time" for gaseous fuel injection with high fuel velocities. Availability of a curve such as figure 11 would make it possible to estimate mixing time without having prerun chugging data available.

11

Computer Simulation

The equations describing the double-dead-time model were programmed on the analog computer and are summarized in appendix C. Stability limits were determined on the computer by doing the following:

(1) Selecting the fuel injector geometry (coefficient) to give the desired fuel injector pressure drop

(2) Setting the oxidizer vaporization time and mixing time to their appropriate values

(3) Varying the oxygen injector orifice coefficient (hence, pressure drop)

(4) Using a closed-loop control, continuously adjust the supply pressure voltages to maintain the desired chamber pressure and flowrates (Table VI gives values of chamber pressure, flow rates, and other pertinent parameters that were used in the simulation and which are averages for all stable runs with the appropriate configuration.)

(5) Recording the values of pressure drop where small perturbations in the system result in steady oscillations in chamber pressure and the observed frequency of those oscillations

(6) Repeating at various fuel injector pressure drop settings with the corresponding delay settings

(7) If necessary, repeating with different values for parameters such as injector capacitance

For the subscale configurations, the oxygen injector capacitance was determined experimentally (ref. 6) to be 7.3×10^{-4} square inch (4.71×10^{-3} cm^2). For the full-scale configurations, values of 0.84×10^{-4} and 1.13×10^{-2} square inch (5.42×10^{-4} and 7.29×10^{-2} cm^2) were calculated in appendix B for standpipe volumes of 775 and 5875 cubic inches (1.27×10^4 and 9.63×10^4 cm^3), respectively.

Because there was no way to calculate the hydrogen velocity through the transpiration-cooled faceplate and because the same trend in frequency with varying injector $\Delta P/P_t$ was observed, the Hersch-Rice drop-size correlation was assumed to apply. If the vaporization time on the computer was varied until a match between simulation and experimentally observed frequencies was obtained, the vaporization time corresponding to a particular transpiration-cooled injector configuration could be determined. For both contraction ratios, this delay was found to be 1.25 times the calculated delay for concentric-tube injection and at the same operating point. When equations (3), (5), and (6) were used, this ratio was translated into a fuel velocity ratio of 0.735.

Simulation Results and Comparison

Figure 12(a) shows the stability boundary obtained on the analog computer for con-

figuration A. Also shown is the experimental boundary determined in figure 8(a) for the 38 runs made with this configuration. Both the experimental and computer frequencies are noted on the figure. Good agreement in boundary shape, position, and frequencies was obtained with the calculated values of delay. Some discrepancies occur at the low values of $\Delta P/P_t$ where errors in readings and cumulative errors in computation can have a significant effect on the data. Difficulties in obtaining unstable data at the low fuel injector $\Delta P/P_t$'s was encountered due to the lower limit on obtainable oxidizer injector ΔP (30 to 40 psi; 20.6 to 27.5 N/cm^2). Use of the Hersch-Rice drop-size correlation with its sensitivity of drop size (hence, vaporization time) to fuel injector velocity (hence, ΔP) closely predicts the observed variation of frequency along the stability boundary.

Figure 12(b) shows a comparison of experimental and computer boundaries for configuration B. Again, the boundary shape and frequencies are closely predicted by the model. It should be noted that this configuration exhibits the higher mode instability, which is characteristic of the model, at fuel injector $\Delta P/P_t$'s around 0.1. Some experimental instabilities around 360 hertz were observed in this region as indicated in the figuse. There is about 10 percent (25 psi; 17.2 N/cm^2) discrepancy in boundary location.

Figure 12(c) shows a comparison of experimental and computer boundaries for configuration C. As previously discussed, the vaporization delay was calculated assuming a velocity through the transpiration-cooled faceplate equal to 74 percent of that which would be obtained with a concentric-tube injector at the same pressure level and flow rate. For the limited amount of data, excellent agreement, in all respects, was obtained with the model.

Figure 12(d) shows a comparison of experimental and computer boundaries for configuration D. As in the previously discussed cases, excellent agreement was obtained using the double-dead-time model. The characteristic higher frequency instability is predicted and observed in the region of 0.1 fuel $\Delta P/P_t$. The assumed reduction in fuel velocity through the transpiration-cooled faceplate satisfies the observed relation between fuel $\Delta P/P_t$ and boundary frequency.

Figure 13 shows the data obtained with the 421-element engine and the computed stability boundaries for the various configurations. It is seen that it would be extremely difficult to achieve unstable operation with the 775-cubic-inch (1.27×10^4-cm^3) standpipe where a pure capacitance is assumed for the simulation and where, in fact, all data obtained with that standpipe lie to the right of their respective boundaries. With a pure capacitive injector standpipe of 5875 cubic inches (0.63×10^4 cm^3), the model indicates that the two data points run with that configuration (H) should have been unstable. However, a more detailed analysis of the standpipe characteristics (appendix B) reveals that the inductance of the standpipe results in a resonant condition around 20 hertz and a high impedance at the frequency of interest (219 Hz), thus coupling the oxidizer feed system (fire valve) pressure drop to that of the injector causing stabilization. The pure capacitive standpipe would have a very low impedance at this frequency, causing a decoupling of

the feed system, as intended. Figure 14 shows the computer-determined effect of stand-pipe neck inductance on the stability of configuration H. The results indicate that unstable operation could not have been obtained with more than 1 or 2 inches of liquid in the neck region during steady-state operation.

SUMMARY OF RESULTS

Low-frequency (chugging) stability limits were determined experimentally for both 1.4-inch- (3.56-cm-) diameter, seven-element and 10.8-inch- (27.4-cm-) diameter, 421-element engine configurations. The propellants were gaseous hydrogen and liquid oxygen. Both propellants were at 140° R (77.8 K). Both the subscale and full-scale configurations were run with the same thrust per element, nozzle contraction ratio, chamber pressure, and mixture ratio. The nominal chamber pressure was 250 psia (172 N/cm^2), and the mixture ratio was maintained at about 5.

Studies were conducted to determine the effect of contraction ratio, chamber length, fuel injection techniques, and oxidizer injector capacitance on the injector pressure requirements for stable engine operation. Experimentally determined stability limits were compared with those predicted using the double-dead-time model.

Unlike the results obtained with single-element injectors (ref. 5), the seven-element testing resulted in a sharp transition from stable to unstable operation as the oxidizer injector pressure drop was lowered. The experimentally determined stability boundaries exhibited a characteristic shape as predicted by the double-dead-time model (ref. 6). The observed chugging frequencies decreased with decreasing fuel injector pressure drop (velocity), indicating a sensitivity of delay (hence, drop size) to fuel velocity as reported in reference 9.

For the subscale configurations tested, very little effect on boundary position (required pressure drop) was noted for changes in contraction ratio or injection method (concentric-tube or transpiration-cooled faceplate). Predictable effects on the observed chugging frequencies were observed. Higher contraction ratios resulted in lower frequencies, due to increases in both the engine time constant and mixing delays.

Good agreement between experimental and computer boundaries was obtained for all subscale configurations. Varporization delay times were calculated using existing vaporization and drop-size correlations (refs. 8 and 9). Vaporization time was found to be a strong function of fuel velocity (pressure drop) for fixed chamber pressure, mixture ratio, and oxidizer injector geometry.

Mixing and reaction times were calculated for all unstable runs using the characteristic equation for the system and the observed chugging frequencies. Average values of 0.2 and 0.5 millisecond were calculated for contraction ratios of 1.9 and 3.0, respectively. Mixing and reaction times were correlated with a selected engine parameter using

available data from engines using the same propellant combination.

The transpiration-cooled injector data were matched by determining, on the analog computer, a fixed ratio between the vaporization times required to give the observed frequencies with both types of injector. Transpiration-cooled data required a 25-percent-higher vaporization time at the same pressure and flow level. Assuming that the Hersch-Rice correlation applies, this would correspond to a fuel velocity equal to 74 percent of that obtained with the concentric-tube injector.

The importance of accurately determining injector impedance was pointed out in the full-scale tests when instabilities were prevented because of feed system coupling effects. Computer results indicate a strong influence of injector capacitance on stability boundary location, shape, and frequencies. A linearlized analysis of the dynamic behavior of the full-scale oxidizer injector standpipe is included in appendix B. This analysis supports the observation of stable operation at extremely low oxidizer injector pressure drops with the full-scale engine.

Lewis Research Center,
    National Aeronautics and Space Administration,
        Cleveland, Ohio, April 8, 1969,
            128-31-51-01-22.

APPENDIX A

SYMBOLS

A   cross-sectional area, in.^{2} (cm^2)

B   liquid bulk modulus, psi (N/cm^2)

C   fluid capacitance, in.^{2} (cm^2)

C_{CT} concentric-tube coefficient

C^* actual characteristic exhaust velocity, $(A_t g P_C)/[(\dot{w}_o + \dot{w}_f)]$, in./sec (cm/sec)

C^*_{th} theoretical characteristic exhaust velocity at nominal mixture ratio, in./sec (cm/sec)

$C^*_{th'}$ theoretical characteristic exhaust velocity at reduced mixture ratio, in./sec (cm/sec)

d   droplet diameter, in. (cm)

d_o oxidizer orifice diameter, in. (cm)

d_f fuel annulus diameter, in. (cm)

f_o observed chugging frequency, Hz

f' simulation chugging frequency, Hz

g   gravitational constant, in./sec^2 (cm/sec^2)

K_{fo} oxidizer feed system coefficient, sec/(in.)(lb mass)$^{1/2}$ (sec/cm-kg$^{1/2}$)

L   fluid inductance, sec^2/in.^{2} (sec^2/cm^2)

l length, in. (cm)

l_{eff} effective chamber length, in. (cm)

M_1 combustion gas Mach number at nozzle inlet

P   absolute pressure, psia (N/cm^2)

ΔP pressure drop, psi (N/cm^2)

R   gas constant, in./^{O}R (cm/K)

r   nominal mixture ratio, $\dot{w}_o/\dot{w}_f$

r' reduced mixture ratio, βr

$\mathscr{S}$ nozzle shape factor

S   Laplacian operator, sec^{-1}

T   fluid temperature, ^{O}R (K)

t   time, sec

V   volume, in.^{3} (cm^3)

v   velocity, in./sec (cm/sec)

$\dot{w}$ mass flow rate, lb mass/sec (kg/sec)

x   distance, in. (cm)

Z   flow impedance, sec/in.^{2} (sec/cm^2)

β fraction vaporized

γ specific heat ratio

ϵ_C contraction ratio, A_c/A_t

θ_g chamber time constant, sec

η combustion efficiency, C^*/C^*_{th}

ρ fluid density, lb mass/in.^{3} (kg/cm^3)

τ time delay, sec

Subscripts:

a   annulus

b   burned products

c	chamber	m	mixing and reaction
cr	critical	N_2	nitrogen
D	droplet	n	nozzle
f	fuel	o	oxidizer
g	gas	r	reduced
i	injected	sp	standpipe
if	fuel injector	t	throat
io	oxidizer injector	to	oxidizer tank
j	center-tube of concentric-tube injector	50	50-percent vaporized
ℓ	liquid		

Superscript:

—   mean value

APPENDIX B

DYNAMIC ANALYSIS OF FULL-SCALE OXIDIZER STANDPIPE

In an attempt to suppress oscillations in the oxidizer injector pressure during chugging, additional volume was added to the injector manifold by placing a standpipe in the system immediately upstream of the injector (see fig. 3). For the initial full-scale testing (configurations E, F, and G), the standpipe was cylindrical with a volume of 775 cubic inches $(1.27\times10^4 \text{ cm}^3)$.

The standpipe was initially filled with gaseous nitrogen at ambient pressure and temperature. Assuming an isentropic compression during the run to the steady-state injector pressure, the capacitance of the compressed gas can be computed from

$$C_g = \frac{p_o V_{sp}}{p_{io} R_{N_2} T_{N_2} \gamma_{N_2}} = 0.84\times10^{-4} \text{ in.}^2 (5.42\times10^{-4} \text{ cm}^2)$$

Since no instabilities could be observed using this standpipe, a larger one having a volume of 5875 cubic inches $(9.62\times10^4 \text{ cm}^3)$ was installed in the system. Figure 15 shows the standpipe geometry and approximate liquid level for an isentropic compression from an initial pressure of 250 psia (172 N/cm^2).

If no frictional losses are assumed, and a lumped-parameter approach is used, the pressure and flow rate in the liquid-filled portion of the standpipe are related as follows:

$$-\frac{\partial p}{\partial x} = \frac{\partial \dot{w}}{A_{sp} \partial t} \quad \text{or} \quad \Delta P = L_l g \frac{d\dot{w}}{dt}$$

$$\frac{\partial p}{\partial t} = -\frac{B}{\rho_l V_{l,sp}} \Delta \dot{w} \quad \text{or} \quad P = \frac{g}{C_l} \int \Delta \dot{w} \, dt$$

In addition, the capacitance due to the trapped gas must be considered in the dynamic analysis. The following values for the capacitance and inductance parameters were calculated for the standpipe shown in figure 15:

Neck, in. (cm)	Capacitance, in.^{2} (cm^2)		Liquid inductance, sec^2/in.^{2} (sec^2/cm^2)
	Liquid	Gaseous	
16 (40.6)	$3.59{\times}10^{-5}$ $(23.2{\times}10^{-5})$	----------	$5.61{\times}10^{-3}$ $(0.870{\times}10^{-3})$
2 (5.08)	$6.18{\times}10^{-5}$ $(39.9{\times}10^{-5})$	----------	$5.10{\times}10^{-5}$ $(0.791{\times}10^{-5})$
54.6 (139)	----------	$1.13{\times}10^{-2}$ $(7.29{\times}10^{-2})$	----------

The electrical analog to the standpipe is shown in figure 16, where S is the Laplacian operator and Z_{sp} is the standpipe flow impedance as indicated. Over the frequency range of interest, the dominant factors are the inductance of the liquid in the neck section and the gas capacitance. The impedance of the standpipe can, therefore, be approximated by a series resonant L-C combination as shown in figure 17.

Figure 18 shows a plot of the magnitude of the standpipe impedance as a function of frequency for both the desired pure capacitance and the attainable resonant cases. The neck was necessary for placement of the control valve (see fig. 3) and for coupling with the feedline. At a frequency of 250 hertz, the resonant circuit has approximately 200 times the impedance of the purely capacitive element required to decouple the feed system from the engine. A pure capacitance of $1.13{\times}10^{-4}$ square inch ($7.29{\times}10^{-4}$ cm^2) is about as effective as the resonant element at the frequency of interest (219 Hz). This value is slightly larger than that obtained with the 775-cubic-inch ($1.27{\times}10^4$ cm^3) standpipe.

APPENDIX C

SUMMARY OF EQUATIONS FOR ANALOG COMPUTER SIMULATION OF

HYDROGEN-OXYGEN ENGINE SYSTEM

The following equations were developed in references 5 and 6 to describe the dynamic behavior of the hydrogen-oxygen rocket engine system and were implemented on the analog computer for this study:

$$P_{if} = \frac{1}{C_f} \int_0^t \left(\overline{\dot{w}}_f - \dot{w}_{if} \right) dt + \overline{P}_{if}$$

$$\dot{w}_{to} = \frac{1}{K_{fo}} \left(\overline{P}_{to} - P_{io} \right)^{1/2}$$

$$P_{io} = \frac{1}{C_{io}} \int_0^t \left(\dot{w}_{to} - \dot{w}_{io} \right) dt + \overline{P}_{io}$$

$$\dot{w}_{io} = \frac{1}{L_{io}} \int_0^t \left[P_{io} - P_c - \frac{\left(\overline{P}_{io} - \overline{P}_c \right)}{\overline{\dot{w}}_o^2} \dot{w}_{io}^2 \right] dt + \overline{\dot{w}}_o$$

$$\dot{w}_{if} = \frac{\overline{\dot{w}}_f}{\left(\overline{P}_{if}^2 - \overline{P}_c^2 \right)^{1/2}} \left(P_{if}^2 - P_c^2 \right)^{1/2}$$

$$\dot{w}_b = \dot{w}_{io}\left(t - \tau_v - \tau_m \right) + \dot{w}_{if}\left(t - \tau_m \right)$$

$$r = \frac{\dot{w}_{io}\left(t - \tau_v - \tau_m \right)}{\dot{w}_{if}\left(t - \tau_m \right)}$$

$$C^* = f(r)$$

$$P_t = \frac{1}{\theta_g} \int_0^t \left(\frac{\eta C_{th}^*}{A_{tg}} \dot{w}_b - P_t \right) dt + \overline{P}_t$$

$$P_c = \frac{\overline{P}_c}{\overline{P}_t} P_t$$

REFERENCES

1. Summerfield, Martin: A Theory of Unstable Combustion in Liquid Propellant Rocket Systems. ARS J., vol. 21, no. 5, Sept. 1951, 11. 108-114.

2. Crocco, Luigi; and Cheng, Sin-I: Theory of Combustion Instability in Liquid Propellant Rocket Motors. AGARDograph No. 8, Butterworths Sci. Publ., 1956.

3. Drain, Daniel I.; Schum, Harold J.; and Wasserbauer, Charles A.: Relations of Combustion Dead Time to Engine Variables for a 20,000-Pound-Thrust Gaseous-Hydrogen - Liquid-Oxygen Rocket Engine. NASA TN D-851, 1961.

4. Heidmann, Marcus F.; Sokolowski, Daniel E.; and Diehl, Lawrence A.: Study of Chugging Instability with Liquid-Oxygen and Gaseous-Hydrogen Combustors. NASA TN D-4005, 1967.

5. Szuch, John R.; and Wenzel, Leon M.: Experimental Verification of a Double Dead-Time Model Describing Chugging in Liquid Bipropellant Rocket Engines. NASA TN D-4564, 1968.

6. Wenzel, Leon M.; and Szuch, John R.: Analysis of Chugging in Liquid-Bipropellant Rocket Engines Using Propellants with Different Vaporization Rates. NASA TN D-3080, 1965.

7. Heidmann, Marcus F.: Oxygen-Jet Behavior During Combustion Instability in a Two-Dimensional Combustor. NASA TN D-2725, 1965.

8. Priem, Richard J.; and Heidmann, Marcus F.: Propellant Vaporization as a Design Criterion for Rocket-Engine Combustion Chambers. NASA TR R-67, 1960.

9. Hersch, Martin; and Rice, Edward J.: Gaseous-Hydrogen-Liquid-Oxygen Rocket Combustion at Supercritical Chamber Pressures. NASA TN D-4172, 1967.

10. Heidmann, Marcus F.; and Wieber, Paul R.: An Analysis of the Frequency Response Characteristics of Propellant Vaporization. Paper presented at the AIAA Second Propulsion Joint Specialist Conference, Colorado Springs, Colorado, June 13-17, 1966.

11. Dankoff, Walter F.; Johnsen, Irving A.; Conrad, E. William; and Tomazic, William A.: M-1 Injector Development-Philosophy and Implementation. NASA TN D-4730, 1968.

TABLE I. - CONFIGURATION A EXPERIMENTAL DATA FOR CONCENTRIC-TUBE INJECTOR

[Number of elements, 7; contraction ratio, 1.96.]

Run	Chamber pressure at injector face, P_c		Liquid oxygen flow rate, $\dot{w}_o$		Gaseous hydrogen flow rate, $\dot{w}_f$		Mixture ratio, r	Combustion efficiency, η_{c*}, percent	Fuel injector pressure drop, ΔP_{if}		Oxidizer injector pressure drop, ΔP_{io}		Chamber pressure at nozzle inlet, P_t		Fuel injector pressure drop ratio, $\Delta P_{if}/P_t$	Liquid oxygen injector pressure drop ratio, $\Delta P_{io}/P_t$	Observed frequency if unstable, f_o, Hz
	psia	N/cm²	lb mass/sec	kg/sec	lb mass/sec	kg/sec	r	percent	psid	N/cm²	psid	N/cm²	psia	N/cm²			
A	265	183	0.670	0.304	0.141	0.064	4.75	97.5	185	127	141	97	251	173	0.736	0.561	---
B	255	176	.653	.296	.132	.060	4.95	97.5	175	121	112	77	242	167	.723	.463	---
C	257	177	.640	.291	.146	.066	4.38	96.5	188	130	88	61	244	168	.771	.361	---
D	265	183	.683	.310	.136	.062	5.02	97.3	175	121	88	61	252	174	.696	.350	---
E	237	163	.592	.269	.139	.063	4.26	95.4	203	140	51	35	225	155	.904	.227	180
F	272	187	.707	.321	.132	.060	5.36	98.7	53	37	159	110	258	178	.204	.614	---
G	267	184	.689	.313	.133	.060	5.18	98.3	58	40	127	88	254	175	.227	.499	---
H	260	179	.672	.305	.129	.059	5.21	98.2	55	38	103	71	246	169	.224	.419	---
I	255	176	.658	.299	.132	.060	4.98	97.0	55	38	71	49	242	167	.227	.293	---
J	259	178	.672	.305	.134	.061	5.02	96.6	56	39	67	46	246	169	.228	.273	---
K	260	179	.665	.302	.132	.060	5.04	98.2	55	38	58	40	247	170	.223	.235	---
L	257	177	.658	.299	.134	.061	4.91	97.3	58	40	54	37	244	168	.238	.221	---
M	260	179	.658	.299	.134	.061	4.91	98.4	55	38	42	29	247	170	.223	.170	---
N	235	162	.646	.293	.146	.066	4.42	87.6	210	145	41	28	223	154	.942	.184	189
O	257	177	.652	.296	.140	.064	4.66	96.5	83	57	70	48	244	168	.340	.287	---
P	260	179	.659	.299	.138	.063	4.78	97.4	80	55	58	40	247	170	.324	.235	---
Q	260	179	.652	.296	.136	.062	4.79	98.7	80	55	54	37	247	170	.322	.217	---
R	258	178	.640	.291	.138	.063	4.64	98.6	78	54	40	28	245	169	.319	.163	140
T	257	177	.690	.313	.131	.059	5.27	94.9	33	23	78	54	244	168	.135	.320	---
U	260	179	.677	.307	.131	.059	5.17	97.3	30	21	61	42	247	170	.122	.247	---
V	256	176	.653	.296	.131	.059	4.98	98.1	32	22	51	35	243	167	.132	.210	---
W	253	174	.646	.293	.129	.059	5.01	98.2	32	22	41	28	240	164	.133	.171	---
X	260	179	.682	.310	.131	.059	5.21	96.8	30	21	46	32	247	170	.122	.186	---
Y	240	165	.646	.293	.125	.057	5.17	94.1	35	24	68	47	228	157	.154	.299	---
Z	235	162	.632	.287	.125	.057	5.06	93.5	35	24	53	37	223	154	.157	.238	---
AA	235	162	.615	.279	.125	.057	4.92	95.2	30	21	45	20	223	154	.135	.202	---
BB	238	164	.622	.282	.123	.056	5.06	96.2	28	19	38	26	226	156	.124	.168	---
CC	230	158	.604	.274	.123	.056	4.91	94.8	25	17	36	25	218	150	.115	.165	---
DD	255	176	.700	.318	.125	.057	5.60	94.9	30	21	153	105	242	167	.124	.632	---
EE	240	165	.659	.299	.142	.064	4.64	89.1	175	121	71	49	228	157	.769	.312	---
FF	225	155	.652	.296	.119	.054	5.48	89.2	305	210	111	76	214	147	1.43	.520	---
GG	205	141	.598	.271	.114	.052	5.25	87.3	330	227	59	41	194	134	1.70	.298	---
GG'	224	154	.598	.271	.114	.052	5.25	95.4	330	227	59	41	213	147	1.46	.182	189
HH	235	162	.652	.296	.133	.060	4.90	89.7	75	52	51	35	223	154	.336	.229	---
II	240	165	.658	.299	.131	.059	5.02	91.5	70	48	51	35	228	157	.307	.224	---
JJ	235	162	.633	.287	.131	.059	4.83	92.0	70	48	39	27	223	154	.314	.175	---
WW	255	176	.634	.288	.137	.062	4.63	98.3	170	117	66	45	242	167	.703	.273	175
XX	268	185	.671	.305	.139	.063	4.83	98.8	152	105	84	58	254	175	.620	.352	---

TABLE II. - CONFIGURATION B EXPERIMENTAL DATA FOR CONCENTRIC-TUBE INJECTOR

[Number of elements, 7; contraction ratio, 3.02.]

Run	Chamber pressure at injector face, P_c		Liquid oxygen flow rate, $\dot{w}_o$		Gaseous hydrogen flow rate, $\dot{w}_f$		Mixture ratio, r	Combustion efficiency, η_{c*}, percent	Fuel injector pressure drop, ΔP_{if}		Oxidizer injector pressure drop, ΔP_{io}		Chamber pressure at nozzle inlet, P_t		Fuel injector pressure drop ratio, $\Delta P_{if}/P_t$	Liquid oxygen injector pressure drop ratio, $\Delta P_{io}/P_t$	Observed frequency if unstable, f_o, Hz
	psia	N/cm^2	lb mass/sec	kg/sec	lb mass/sec	kg/sec			psid	N/cm^2	psid	N/cm^2	psia	N/cm^2			
1	233	161	0.408	0.185	0.104	0.047	3.92	91.0	272	187	27	19	228	157	1.34	0.113	135
2	233	161	.408	.185	.104	.047	3.92	91.0	272	187	27	19	228	157	1.34	.113	140
3	247	170	.440	.200	.104	.047	4.23	91.5	248	171	42	29	242	167	1.11	.167	149
4	283	195	.482	.219	.0970	.0440	4.97	96.5	192	132	61	42	277	191	.693	.220	---
5	275	189	.463	.210	.0970	.0440	4.77	96.4	200	138	46	32	269	185	.743	.171	---
6	260	179	.439	.199	.0877	.0398	5.01	97.5	95	65	51	35	254	175	.373	.201	---
7	248	171	.433	.197	.0885	.0402	4.89	97.5	107	74	31	21	243	167	.449	.126	127
8	258	178	.439	.199	.0980	.0445	4.48	97.5	87	60	36	25	253	174	.361	.139	136
9	268	185	.439	.199	.0970	.0440	4.53	97.4	77	53	36	25	262	181	.294	.137	114
10	265	183	.439	.199	.0935	.0424	4.70	97.4	75	52	42	29	259	178	.289	.162	---
11	267	184	.439	.199	.0920	.0418	4.77	98.6	83	57	50	34	261	180	.319	.192	---
12	273	188	.463	.210	.0880	.0400	5.26	98.7	35	24	67	46	267	184	.132	.252	---
13	266	183	.445	.202	.0880	.0400	5.06	98.9	39	27	46	32	260	179	.149	.176	---
14	270	186	.449	.204	.0900	.0409	4.99	98.8	33	23	32	22	264	182	.127	.104	---
15	263	181	.439	.199	.0911	.0414	4.82	97.5	35	24	24	17	257	177	.136	.093	105 360
16	265	183	.451	.205	.0928	.0421	4.86	95.9	33	23	20	14	259	178	.127	.077	110 360
17	268	185	.445	.202	.0928	.0421	4.80	97.8	30	21	19	13	262	181	.114	.072	114 360

TABLE III. - CONFIGURATION C EXPERIMENTAL DATA FOR TRANSPIRATION-COOLED INJECTOR

[Number of elements, 7; contraction ratio, 1.96.]

Run	Chamber pressure at injector face, P_c		Liquid oxygen flow rate, $\dot{w}_o$		Gaseous hydrogen flow rate, $\dot{w}_f$		Mixture ratio, r	Combustion efficiency, η_{c*}, percent	Fuel injector pressure drop, ΔP_{if}		Oxidizer injector pressure drop, ΔP_{io}		Chamber pressure at nozzle inlet, P_t		Fuel injector pressure drop ratio, $\Delta P_{if}/P_t$	Liquid oxygen injector pressure drop ratio, $\Delta P_{io}/P_t$	Observed frequency if unstable, f_o, Hz
	psia	N/cm^2	lb mass/sec	kg/sec	lb mass/sec	kg/sec			psid	N/cm^2	psid	N/cm^2	psia	N/cm^2			
KK	273	188	0.700	0.318	0.140	0.064	5.00	97.7	162	112	153	105	259	178	0.625	0.591	---
LL	267	184	.671	.305	.140	.064	4.72	97.9	143	99	97	67	253	174	.565	.383	---
MM	265	183	.659	.299	.142	.064	4.64	98.5	141	97	74	51	252	174	.559	.293	122
NN	263	181	.652	.296	.140	.064	4.59	98.2	163	112	75	52	249	172	.656	.302	134
OO	258	178	.665	.302	.129	.059	5.16	98.1	162	112	77	53	245	169	.663	.316	112
PP	260	179	.665	.302	.129	.059	5.16	98.8	60	41	77	53	246	169	.245	.314	99
QQ	253	174	.657	.298	.123	.056	5.34	98.5	37	25	81	56	240	165	.156	.339	---
RR	246	169	.628	.285	.123	.056	5.11	98.6	34	23	56	39	233	161	.148	.243	97
SS	243	167	.615	.278	.123	.056	5.00	99.0	32	22	52	36	231	159	.139	.225	---

TABLE IV. - CONFIGURATION D EXPERIMENTAL DATA FOR TRANSPIRATION-COOLED INJECTOR

[Number of elements, 7; contraction ratio, 3.02.]

Run	Chamber pressure at injector face, P_c		Liquid oxygen flow rate, $\dot{w}_o$		Gaseous hydrogen flow rate, $\dot{w}_f$		Mixture ratio, r	Combustion efficiency, η_{c*}, percent	Fuel injector pressure drop, ΔP_{if}		Oxidizer injector pressure drop, ΔP_{io}		Chamber pressure at nozzle inlet, P_t		Fuel injector pressure drop ratio, $\Delta P_{if}/P_t$	Liquid oxygen injector pressure drop ratio, $\Delta P_{io}/P_t$	Observed frequency if unstable, f_o, Hz
	psia	N/cm²	lb mass/sec	kg/sec	lb mass/sec	kg/sec			psid	N/cm²	psid	N/cm²	psia	N/cm²			
24	270	186	0.421	0.191	0.123	0.056	3.42	98.4	275	189	38	26	264	182	1.24	0.134	142
25	285	196	.463	.210	.117	.053	3.96	94.4	225	155	56	39	279	192	.807	.201	---
26	285	196	.467	.212	.112	.051	4.17	95.0	195	134	57	39	279	192	.700	.205	---
27	293	202	.427	.194	.145	.066	2.94	97.5	237	163	57	39	286	197	.828	.199	149
28	274	189	.482	.219	.0825	.0375	5.84	98.9	66	45	67	46	268	185	.244	.248	---
29	246	169	.421	.191	.102	.046	4.13	94.5	99	68	29	20	241	166	.452	.115	112
30	263	181	.439	.199	.0942	.0428	4.66	96.5	80	55	32	22	257	177	.311	.124	100
31	276	190	.463	.210	.0956	.0434	4.84	97.2	74	51	46	32	270	186	.274	.170	---
32	275	189	.469	.213	.0874	.0397	5.37	98.9	30	21	48	33	269	185	.111	.178	---
33	262	181	.445	.202	.0844	.0383	5.27	98.7	35	24	40	28	256	176	.137	.156	---
34	258	178	.445	.202	.0891	.0405	4.99	95.4	27	19	26	18	252	174	.107	.103	77 360
35	245	169	.452	.205	.0872	.0396	5.18	90.3	30	21	20	14	240	165	.125	.083	79 360
36	264	182	.439	.199	.0921	.0418	4.77	97.5	31	21	32	22	258	178	.120	.124	---
37	264	182	.445	.202	.0873	.0396	5.10	98.4	46	32	57	39	259	178	.176	.219	---
38	255	176	.433	.197	.0930	.0422	4.66	94.8	30	21	25	17	249	172	.120	.100	79 360
39	265	183	.445	.202	.0950	.0431	4.68	96.0	40	28	26	18	259	178	.154	.100	77 398
40	275	189	.457	.207	.0946	.0429	4.83	98.0	30	21	34	23	269	185	.112	.126	79 391
41	278	192	.475	.216	.0893	.0405	5.32	98.4	77	53	49	34	272	187	.283	.180	---
45	273	188	.451	.205	.0964	.0438	4.68	97.6	37	25	33	23	267	184	.139	.124	77
46	268	185	.451	.205	.0973	.0442	4.64	95.4	27	19	24	17	262	181	.104	.093	77 360

TABLE V. - FULL-SCALE ENGINE EXPERIMENTAL DATA FOR CONCENTRIC-TUBE INJECTOR

[Number of elements, 421.]

Configu-ration	Contrac-tion ratio, ϵ_c	Chamber length, l_c		Standpipe volume, V_o		Chamber pressure at injector face, P_c		Liquid oxygen flow rate, w_o		Mixture ratio, r	Chamber pressure at nozzle inlet, P_t		Fuel injector pressure drop ratio, $\Delta P_{if}/P_t$	Liquid oxygen injector pressure drop ratio, $\Delta P_{io}/P_t$
		in.	cm	in.^{3}	cm^3	psia	N/cm^2	lb mass/sec	kg/sec		psia	N/cm^2		
E	1.9	10.5	26.7	775	12 710	262	181	43.2	19.6	5.13	248	171	1.10	0.390
E						262	181	45.7	20.7	5.00	248	171	1.14	.317
E						273	188	45.6	20.7	4.90	258	178	1.04	.302
E						276	190	46.1	20.9	4.94	261	180	1.10	.218
F	3.0					293	202	32.2	14.6	4.98	287	198	.339	.125
F						267	184	27.3	12.4	5.12	262	181	.315	.0802
F						265	183	27.3	12.4	5.12	260	179	.326	.0423
G		5.0	12.7			274	189	29.0	13.2	5.16	268	185	1.85	.0776
G						231	159	29.0	13.2	4.99	226	156	2.13	.206
G						255	176	38.3	17.4	5.05	250	172	2.04	.113
H				5875	96 350	220	152	18.9	8.6	3.18	216	149	2.16	.0504
H				5875	96 350	219	151	22.1	10.0	3.78	214	147	2.10	.0607

TABLE VI. – SELECTED STEADY-STATE VALUES FOR ANALOG COMPUTER SIMULATION

[Mixture ratio, 5.0.]

	Configuration					
	A, C	E	B, D	F	G	H
Contraction ratio, $\epsilon_c = 1.97$						
Chamber pressure at nozzle inlet, $\overline{P}_t$, psia (N/cm^2)	240 (165)	240 (165)	------------	------------	------------	------------
Total oxidizer flow rate, $\overline{w}_o$, lb mass/sec (kg/sec)	0.650 (0.295)	39.1 (17.8)	------------	------------	------------	------------
Engine time constant, θ_g, msec	0.576	0.818	------------	------------	------------	------------
Oxidizer injector inductance, $\mathscr{L}_o$, sec^2/in.^{2} (sec^2/m^2)	0.0754 (116.9)	0.00158 (2.45)	------------	------------	------------	------------
Oxidizer feed system impedance coefficient, K_{fo}, (sec)(in.$^{-1}$)(lb mass$^{-1/2}$) ((sec)(cm^{-1})(kg$^{-1/2}$))	17.34 (10.14)	0.568 (0.332)	------------	------------	------------	------------
Oxidizer injector capacitance, C_o, in.^{2} (cm^2)	7.3×10^{-4} (47.1×10^{-4})	8×10^{-4} (5.16×10^{-4})	------------	------------	------------	------------
Momentum pressure loss ratio, $\overline{P}_c/\overline{P}_t$	1.053	1.053	------------	------------	------------	------------
Fuel injector capacitance, C_f, in.^{2} (cm^2)	1.67×10^{-4} (10.77×10^{-4})	1.67×10^{-4} (10.77×10^{-4})	------------	------------	------------	------------
Contraction ratio, $\epsilon_c = 3.08$						
Chamber pressure at nozzle inlet, $\overline{P}_t$, psia (N/cm^2)	------------	------------	260 (179)	260 (179)	260 (179)	260 (179)
Total oxidizer flow rate, $\overline{w}_o$, lb mass/sec (kg/sec)	------------	------------	0.450 (0.204)	27.03 (12.3)	27.03 (12.3)	27.03 (12.3)
Engine time constant, θ_g, msec	------------	------------	0.893	1.28	0.905	0.905
Oxidizer injector inductance, $\mathscr{L}_o$, sec^2/in.^{2} (sec^2/m^2)	------------	------------	0.0754 (116.9)	0.00158 (2.45)	0.00158 (2.45)	0.00158 (2.45)
Oxidizer feed system impedance coefficient, K_{fo}, (sec)(in.$^{-1}$)(lb mass$^{-1/2}$) ((sec)(cm^{-1})(kg$^{-1/2}$))	------------	------------	17.34 (10.14)	0.803 (0.470)	0.803 (0.470)	0.803 (0.470)
Oxidizer injector capacitance, C_o, in.^{2} (cm^2)	------------	------------	7.3×10^{-4} (47.1×10^{-4})	0.8×10^{-4} (5.16×10^{-4})	0.8×10^{-4} (5.16×10^{-4})	1.0×10^{-2} (6.45×10^{-4})
Momentum pressure loss ratio, $\overline{P}_c/\overline{P}_t$	------------	------------	1.021	1.021	1.021	1.021
Fuel injector capacitance, C_f, in.^{2} (cm^2)	------------	------------	1.67×10^{-4} (10.77×10^{-4})	1.67×10^{-4} (10.77×10^{-4})	1.67×10^{-4} (10.7×10^{-4})	1.67×10^{-4} (10.7×10^{-4})
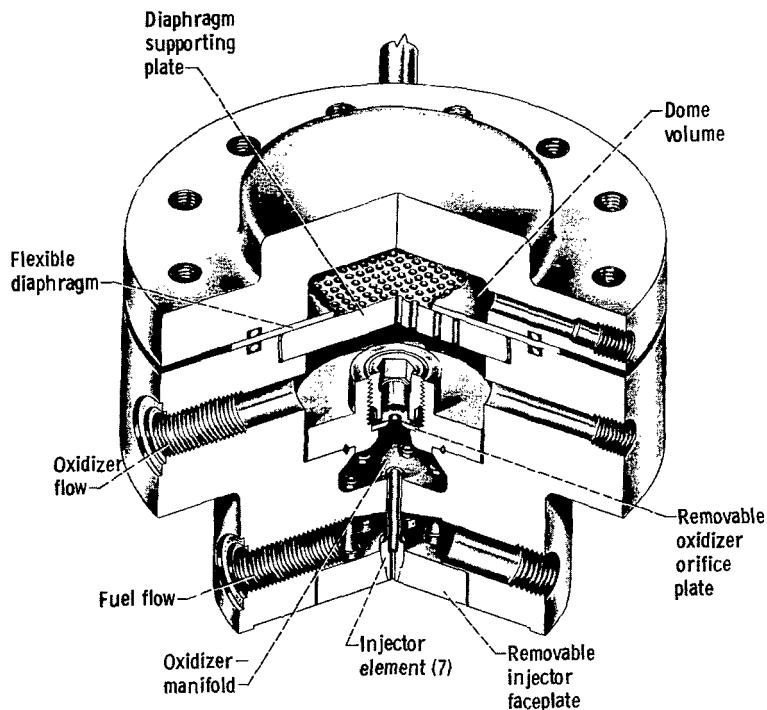
Figure 1. - Cutaway view of subscale engine injector.
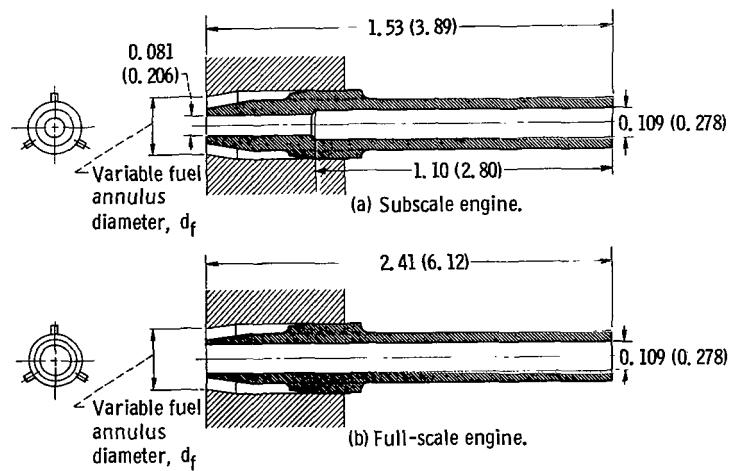
Figure 2. - Concentric-tube injector element detail. All dimensions are in inches (cm).
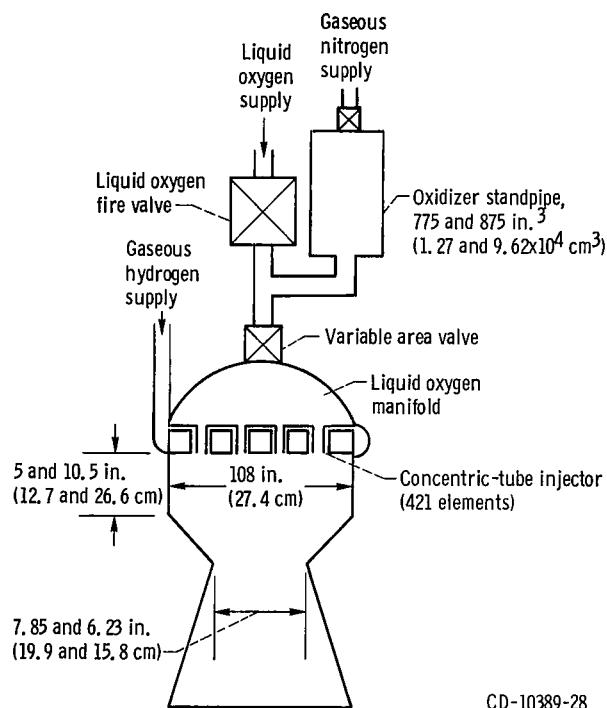
Figure 3. – Full-scale engine configuration.

CD-10389-28
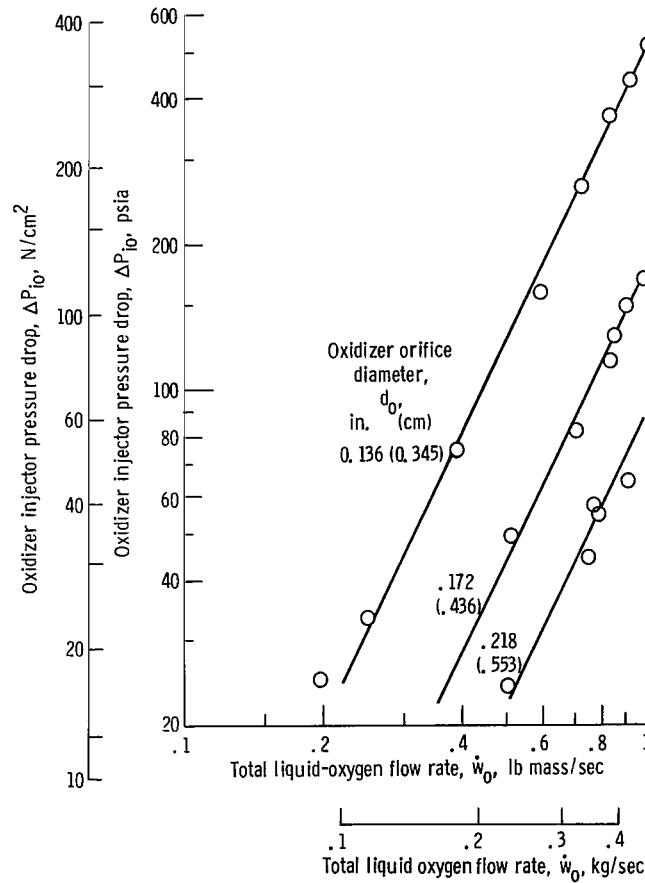
Figure 4. – Cold-flow oxidizer injector calibration for various orifice diameters. Subscale engine.
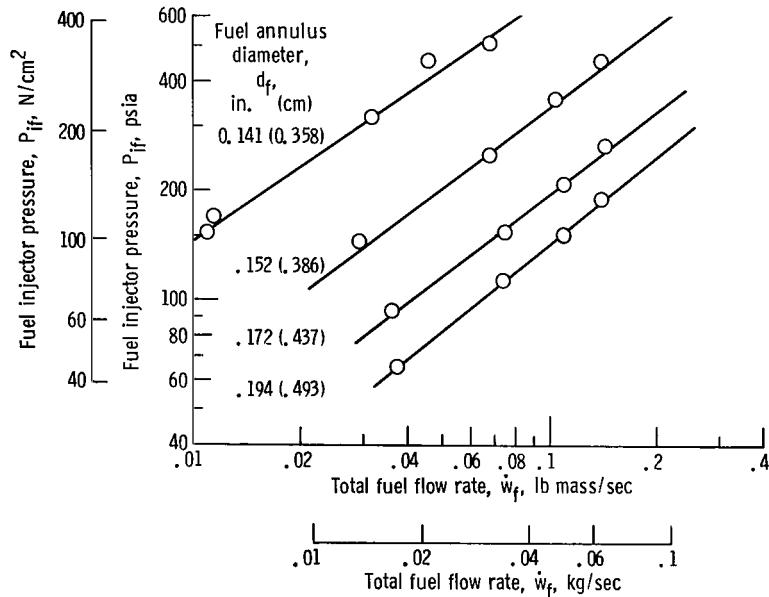
Figure 5. - Cold-flow fuel injector pressure as function of flow rate for various annulus diameters. Back pressure, 15 psia (10.3 N/cm²); subscale engine.
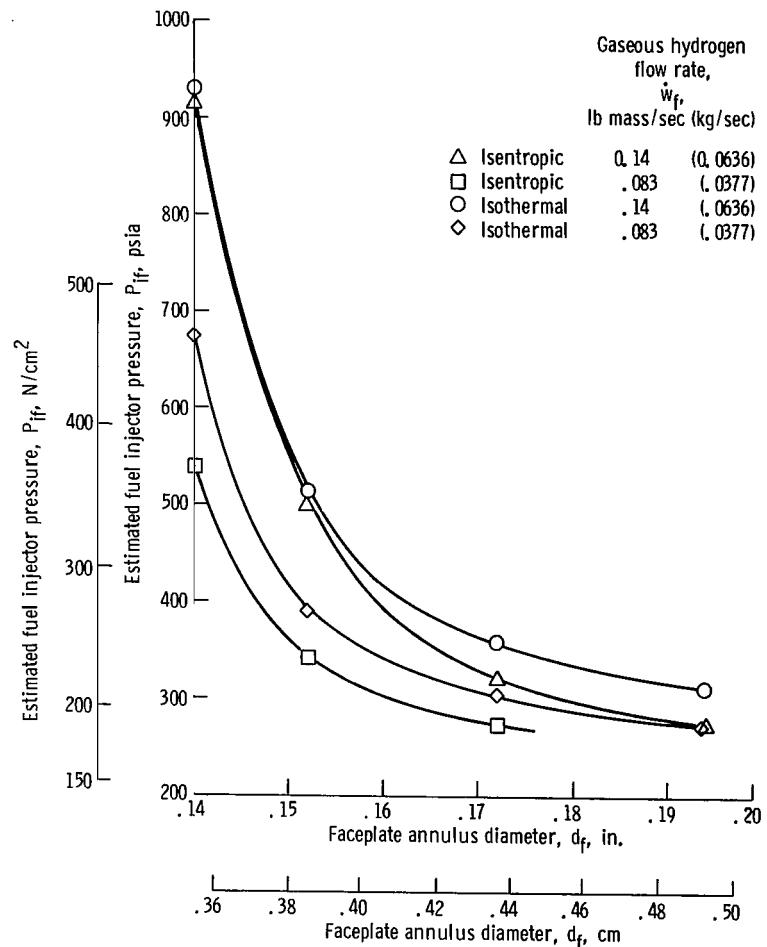

Figure 6. - Estimated fuel injector pressures as function of annulus diameter at nominal flow rates and back pressure of 250 psia (172 N/cm²) subscale engine.
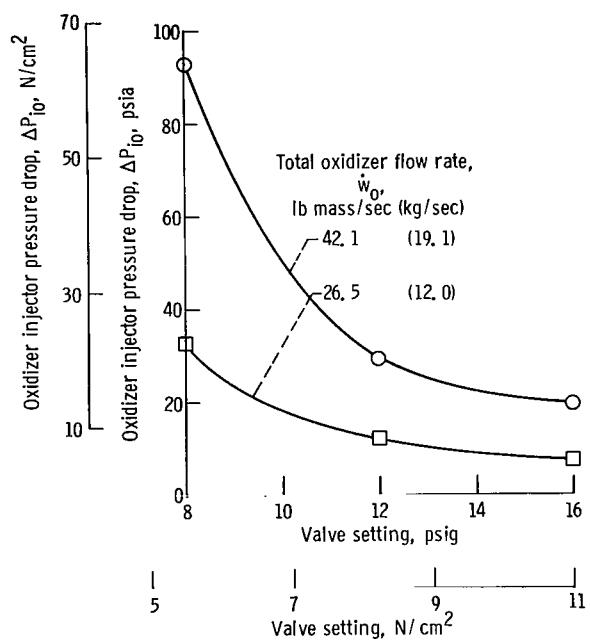
Figure 7. – Cold-flow calibration of full-scale variable-area valve-injector combination.
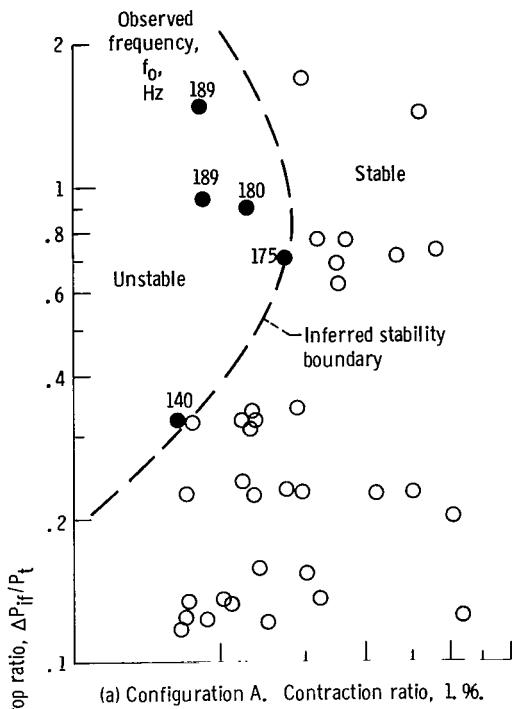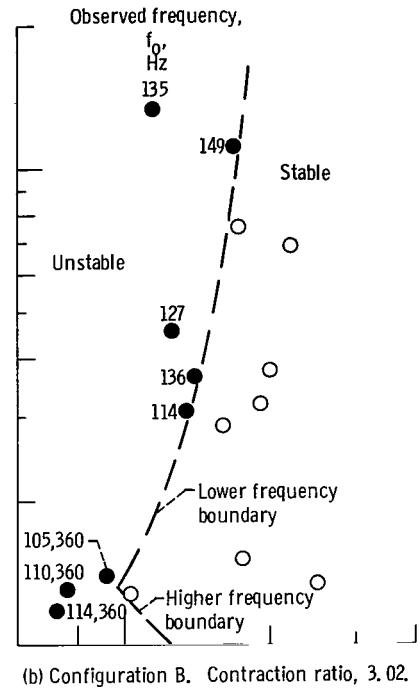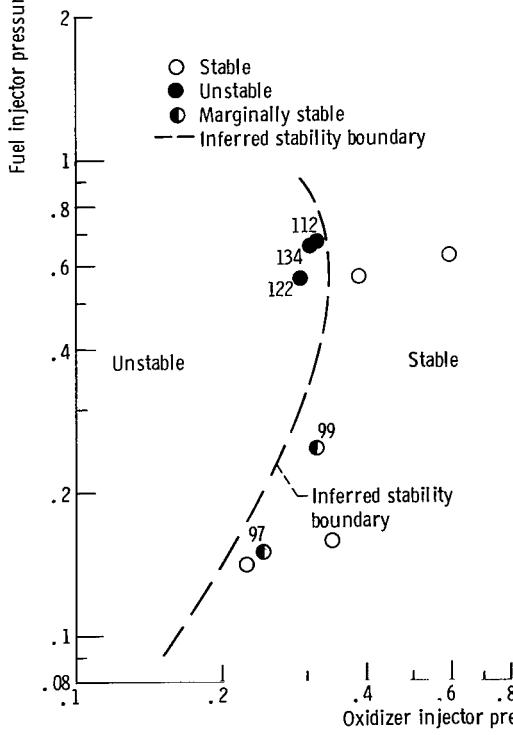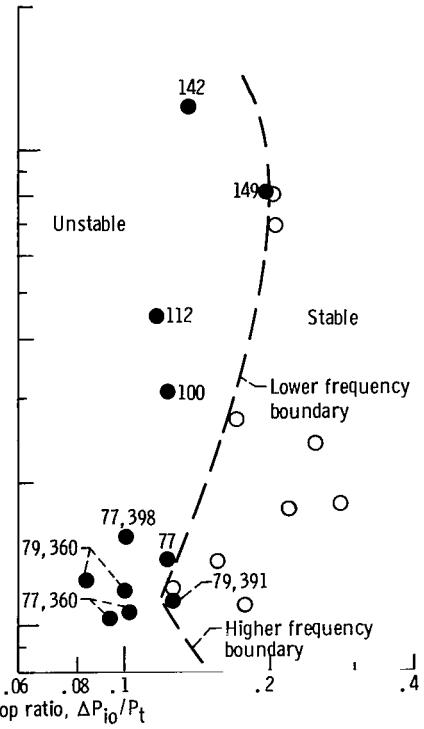
Figure 8. - Experimental data and inferred stability boundary for concentric-tube injector. Number of elements, 7.
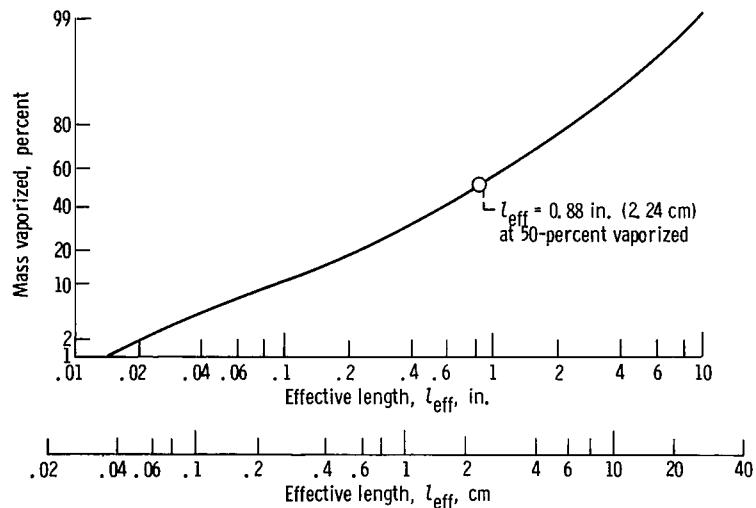
Figure 9. – Priem-Heidmann effective length correlation for oxygen sprays. Geometric; standard deviation of spray, 2.3.
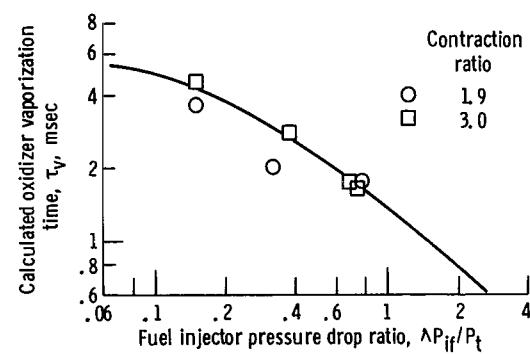
Figure 10. – Effect of fuel injector pressure drop on oxidizer vaporization time using Priem-Heidman effective length parameter and Hersch-Rice drop-size correlation.
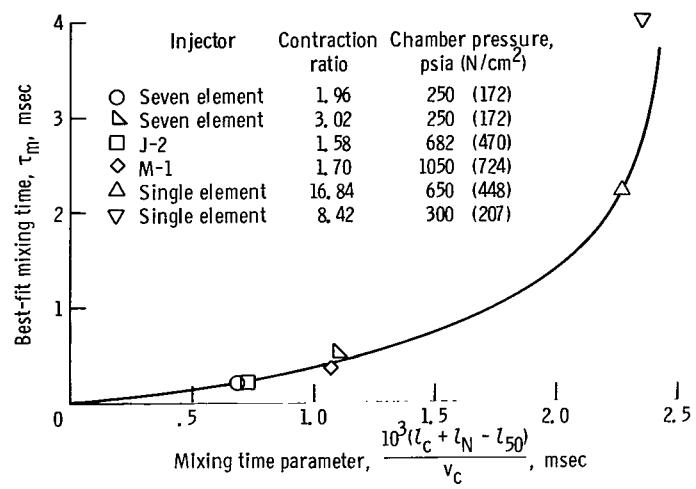
Figure 11. - Mixing time correlation.
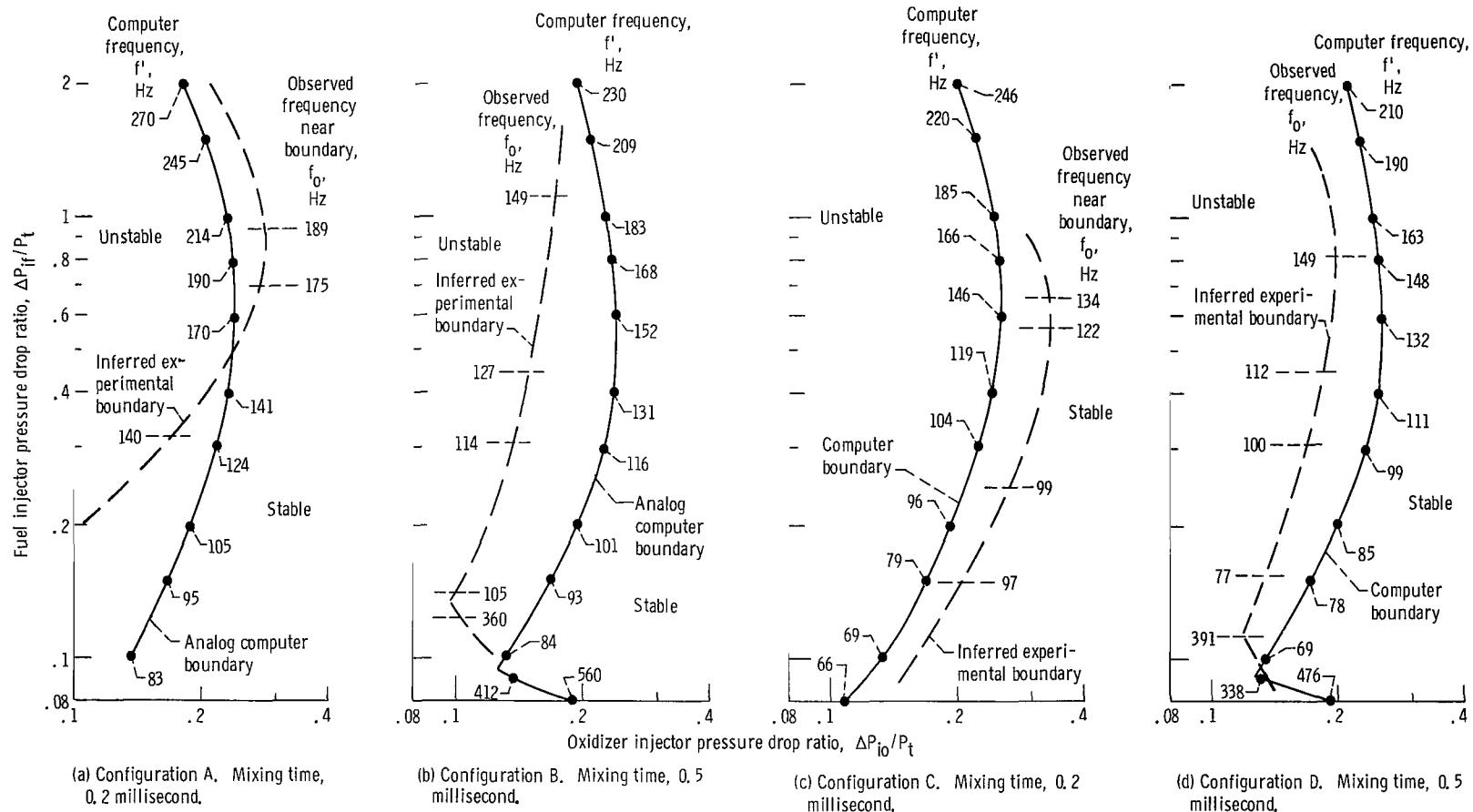
Figure 12. – Comparison of experimental and computer boundaries.

(a) Effect of contraction ratio.

(b) Effect of standpipe volume.
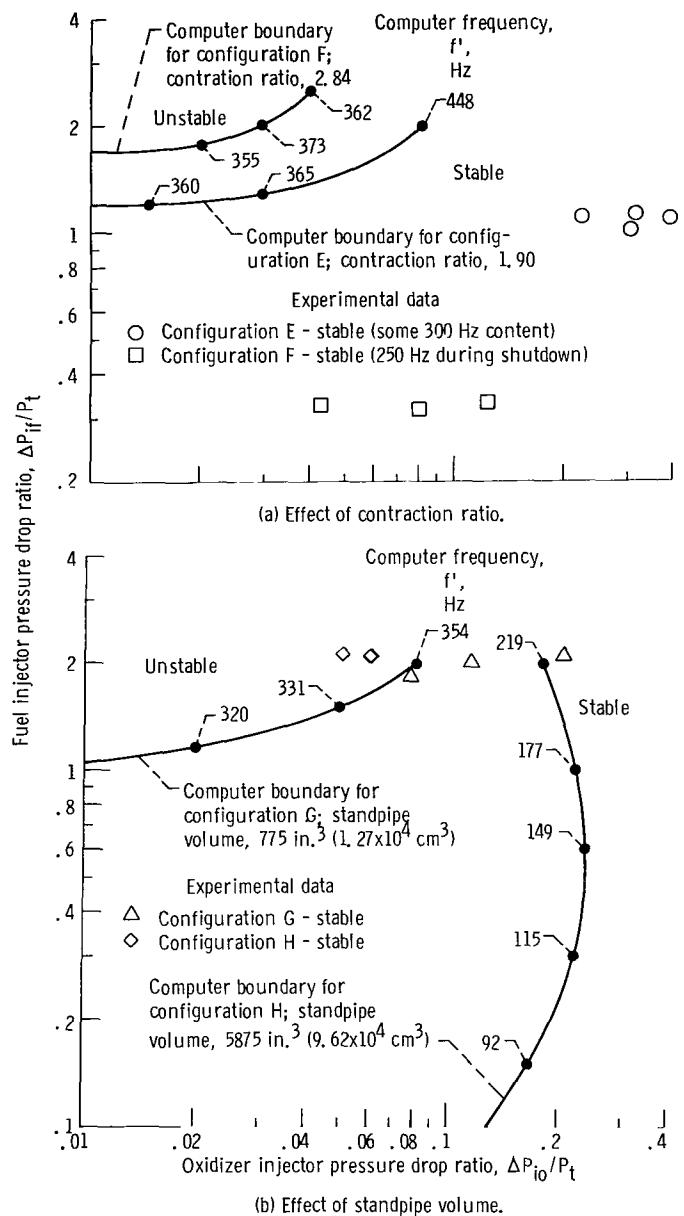
Figure 13. – Comparison of full-scale experimental and computer data assuming pure capacitive oxidizer manifold.

A = 101.6 in.^{2} (655 cm^2)

Gas

56.6 in.
(144 cm)

2 in.
(5.08 cm)

16 in.
(40.6 cm)

A = 7.39 in.^{2} (47.6 cm^2)
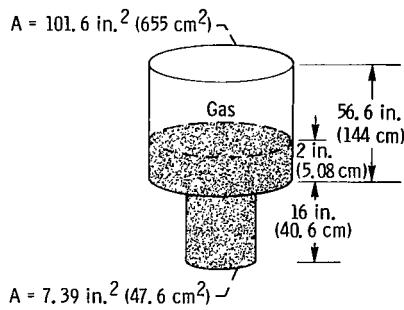
Figure 15. - Geometry of 5875 cubic inch
(9.62x10^4 cm^3) standpipe.
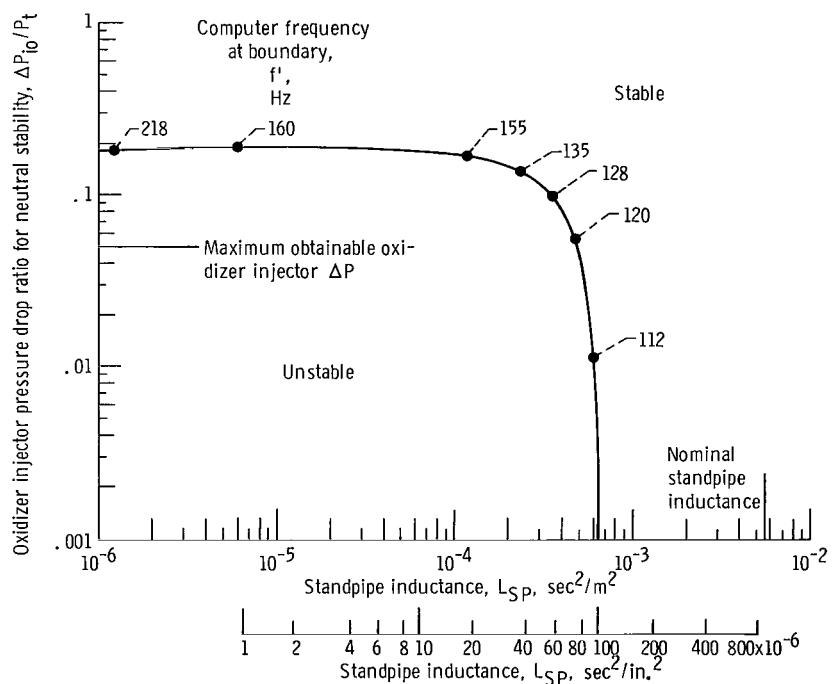
Figure 14. - Effect of standpipe inductance on engine stability for configuration H as
determined on analog computer. Fuel injector pressure drop ratio, 2; oxidizer
standpipe capacitance, 1.13x10^{-2} square inch (7.29x10^{-2} cm^2); mixing time,
0.5 millisecond.

37

Neck liquid
inductance
5.61×10^{-3} S
$(0.871 \times 10^{-3}$ S)

2-Inch
(5.04-cm) liquid
level inductance
5.10×10^{-5} S
$(0.791 \times 10^{-5}$ S)

2-Inch (5.04-cm)
liquid level capacitance
$\dfrac{1}{6.18 \times 10^{-5}}$ S $\dfrac{1}{(39.8 \times 10^{-5}}$ S)

Neck
capacitance
$\dfrac{1}{3.59 \times 10^{-5}}$ S
$\dfrac{1}{(23.2 \times 10^{-5}}$ S)

Gas capacitance
$\dfrac{1}{1.13 \times 10^{-2}}$ S $\dfrac{1}{(7.29 \times 10^{-2}}$ S)

Standpipe flow impedance,
$Z_{SP}(S)$,
$sec/in.^2$ (sec/cm^2) $\longrightarrow$
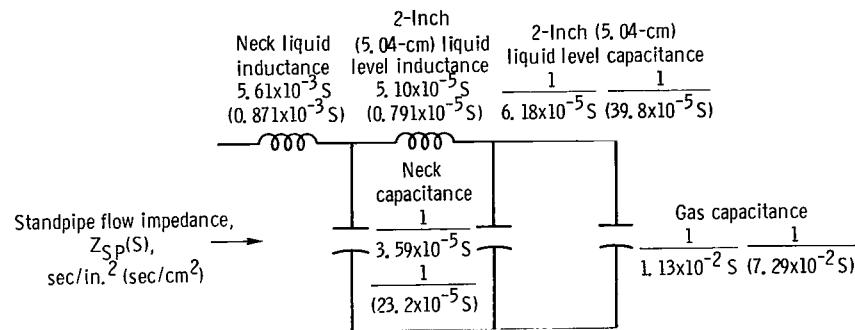
Figure 16. - Electrical analog of standpipe at nominal operating conditions.

5.66×10^{-3} S
$(0.879 \times 10^{-3}$ S)

Standpipe flow
impedance, $Z_{SP}(S)$ $\longrightarrow$

$\dfrac{1}{1.13 \times 10^{-2}}$ S $\dfrac{1}{(7.29 \times 10^{-2}}$ S)
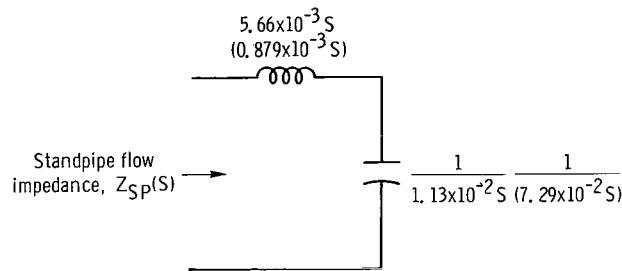
Figure 17. - Approximate analog of standpipe over frequency range of interest.
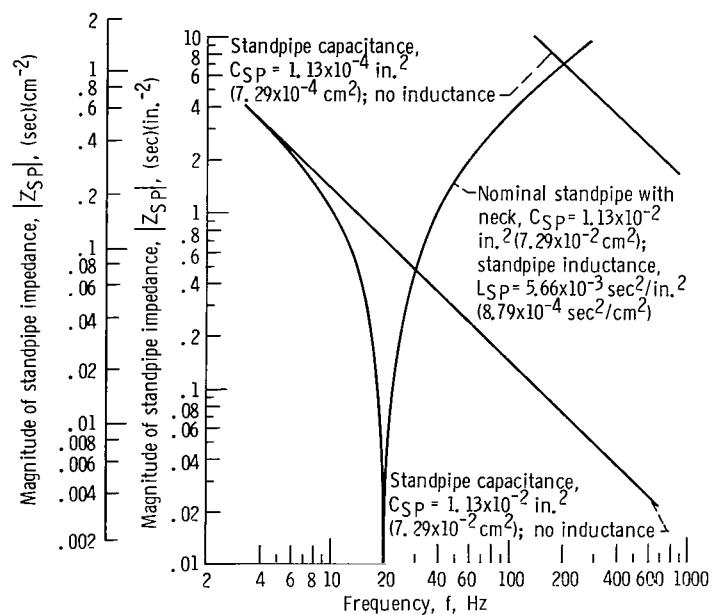
Figure 18. - Magnitude of standpipe impedance as function of frequency for capacitive and resonant configurations.

38
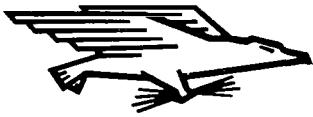
01U 001 53   51 3DS   69163   00903
AIR FORCE WEAPONS LABORATORY/AFWL/
KIRTLAND AIR FORCE BASE, NEW MEXICO 8711

ATT E. LOU BOWMAN, ACTING CHIEF TECH. LI

"*The aeronautical and space activities of the United States shall be
conducted so as to contribute . . . to the expansion of human knowl-
edge of phenomena in the atmosphere and space. The Administration
shall provide for the widest practicable and appropriate dissemination
of information concerning its activities and the results thereof.*"

— NATIONAL AERONAUTICS AND SPACE ACT OF 1958

NASA SCIENTIFIC AND TECHNICAL PUBLICATIONS

TECHNICAL REPORTS: Scientific and
technical information considered important,
complete, and a lasting contribution to existing
knowledge.

TECHNICAL NOTES: Information less broad
in scope but nevertheless of importance as a
contribution to existing knowledge.

TECHNICAL MEMORANDUMS:
Information receiving limited distribution
because of preliminary data, security classifica-
tion, or other reasons.

CONTRACTOR REPORTS: Scientific and
technical information generated under a NASA
contract or grant and considered an important
contribution to existing knowledge.

TECHNICAL TRANSLATIONS: Information
published in a foreign language considered
to merit NASA distribution in English.

SPECIAL PUBLICATIONS: Information
derived from or of value to NASA activities.
Publications include conference proceedings,
monographs, data compilations, handbooks,
sourcebooks, and special bibliographies.

TECHNOLOGY UTILIZATION
PUBLICATIONS: Information on technology
used by NASA that may be of particular
interest in commercial and other non-aerospace
applications. Publications include Tech Briefs,
Technology Utilization Reports and Notes,
and Technology Surveys.

Details on the availability of these publications may be obtained from:

SCIENTIFIC AND TECHNICAL INFORMATION DIVISION

NATIONAL AERONAUTICS AND SPACE ADMINISTRATION
Washington, D.C. 20546